Airborne Sensing for Ship Air Wake Surveys with a Tethered Autonomous UAV

Andrew J. Torgesen* and Jonathan P. How†
Massachusetts Institute of Technology, Cambridge, Massachusetts, 02139

Benjamin Cameron‡
Creare LLC, Hanover, New Hampshire, 03755, USA

Obtaining experimental air flow data for validating computational models of ship air wakes is critical to addressing current challenges associated with recovering maritime aircraft using naval vessels. Small unmanned aircraft are desirable for this task due to their maneuverability and minimal invasiveness in terms of installation and usage. This paper presents a small, tethered, unmanned aircraft system capable of providing high-resolution air wake measurements behind a moving maritime vessel under a wide variety of wind conditions. The air wake measurement task is accomplished by having the aircraft autonomously sweep behind the moving vessel at various altitudes while collecting both air flow data from an omnidirectional probe and relative state measurements. Relative state measurements are obtained through a sensor fusion scheme involving differential GPS and vision-based pose measurements from an infrared beacon array mounted on the ship deck. The proposed system is able to deduce both the steady-state and turbulent components of the air wake stream as a function of position relative to the ship without the need for rigorous sensor calibration. Results demonstrating the robustness of the tethered flight and relative state estimation schemes to a relative wind speed of up to 10 m/s are obtained with motion-capture-validated simulation testing as well as indoor testing in hardware. Near-term future work will include conducting outdoor field experiments to show the effectiveness of the platform as a high-resolution in-situ air wake measurement system.

I. Nomenclature

$\check{\boldsymbol{x}}$	=	Desired state to be tracked with a controller
$\hat{\boldsymbol{x}}$	=	Estimated state
$\boldsymbol{x}$	=	True state
$\tilde{\boldsymbol{x}}$	=	Error-state, representing $\check{\boldsymbol{x}} - \hat{\boldsymbol{x}}$ for control or $\boldsymbol{x} - \hat{\boldsymbol{x}}$ for estimation
${}^{\mathcal{B}}\boldsymbol{f}_{\text{ext}},\ {}^{\mathcal{B}}\hat{\boldsymbol{f}}_{\text{ext}}$	=	Actual and estimated external force acting on UAV, expressed in UAV body-fixed frame
${}^{\mathcal{B}}f_{\text{ext,thresh}}$	=	Threshold external force scalar value for deducing tether tautness
$R(\boldsymbol{q})$	=	Rotation matrix equivalent of quaternion $\boldsymbol{q}$
$[\cdot]_\times$	=	Matrix skew operator
g	=	Gravitational acceleration = 9.81 m/s^2
m	=	UAV mass
f_{thrust}	=	Thrust force generated by UAV propellers
${}^{\mathcal{I}}\boldsymbol{p}_{\mathcal{B}/\mathcal{I}}$	=	Position of UAV relative to inertial frame origin, expressed in inertial frame
$\boldsymbol{q}_{\mathcal{I}}^{\mathcal{B}}$	=	Quaternion representing passive rotation of the UAV body frame with respect to (w.r.t.) the inertial frame
${}^{\mathcal{B}}\boldsymbol{v}_{\mathcal{B}/\mathcal{I}}$	=	Velocity of UAV with respect to inertial frame, expressed in UAV body frame
$\boldsymbol{\beta}_a,\ \boldsymbol{\beta}_\omega,\ \beta_b$	=	Accelerometer, gyro, and barometer biases
${}^{\mathcal{S}}\boldsymbol{p}_{\mathcal{B}/\mathcal{S}}$	=	Position of UAV relative to ship-fixed frame origin, expressed in ship-fixed frame
$\boldsymbol{q}_{\mathcal{S}}^{\mathcal{B}}$	=	Quaternion representing passive rotation from ship frame to UAV body frame
$\boldsymbol{q}_{\mathcal{I}}^{\mathcal{S}}$	=	Quaternion representing passive rotation from inertial frame to ship frame

*Graduate Research Assistant, Massachusetts Institute of Technology Department of Aeronautics and Astronautics.
†Richard Cockburn Maclaurin Professor, Massachusetts Institute of Technology Department of Aeronautics and Astronautics.
‡UAS Group Lead, Creare LLC.

${}^{\mathcal{I}}\boldsymbol{v}_{\mathcal{S}/\mathcal{I}}$	=	Velocity of ship frame with respect to inertial frame, expressed in inertial frame
$\boldsymbol{a}_m,\ \boldsymbol{\omega}_m$	=	IMU accelerometer and gyro measurements
$\boldsymbol{\eta}_a,\ \boldsymbol{\eta}_\omega$	=	True IMU accelerometer and gyro errors
$(\cdot)_k^-$	=	Prior belief distribution at time step k
$(\cdot)_k^+$	=	Posterior belief distribution at time step k
Q_k	=	Filter covariance matrix at time step k
$\boldsymbol{y}_k = h(\boldsymbol{x}_k)$	=	Sensor measurement model
$W_k,\ V_k$	=	Process and sensor noise covariance matrices at time step k
$k_f,\ k_\beta$	=	Vehicle-specific rotor blade drag coefficients

II. Introduction

A considerable challenge posed to the takeoff and landing of maritime aircraft on a moving ship stems from having to stabilize in the midst of a wake of turbulent airflow traversing the flight deck area. This region of turbulent air wake flow arises in the lee of the ship's superstructure as it interacts with a relative headwind. Because of the inherent risk that the air wake poses to stability during close-proximity flight, ongoing efforts are being made to use Computational Fluid Dynamics (CFD) models to accurately characterize the air wake profile for different classes of navy vessels [1–4] as well as to quantitatively determine the effect of air wakes on aircraft dynamics [5–7]. Despite their prevalence, these models based on CFD analysis benefit greatly from experimental validation through in-situ air wake velocity measurement.

Small unmanned air vehicles (UAV) for air wake measurement on naval vessels represent an attractive alternative to deck-mounted anemometers and scale-model wind tunnel testing due to their ability to operate in the vicinity of the ship while also capturing air wake effects behind the ship and over the water. These vehicles require relatively little setup and interference with existing naval vessel configurations which are already designed to accommodate aircraft. Flight experiments with remotely piloted air vehicles in the wake of maritime vessels such as [8] have provided a proof of concept for the usage of such vehicles as air wake measurement devices.

In recent years, there have been several attempts to obtain experimental measurements of the spatially varying air wake velocity profile using small UAVs for the purpose of validating CFD simulations. Phelps et al. [9] employed the use of a small RC plane with known aerodynamic coefficients and a small sensor suite consisting of an inertial measurement unit (IMU), GPS, and a GPS mounted on the ship. While their experiments demonstrated that air wake measurements could be obtained with an inexpensive platform, the inherent limitations in the sensor suite and ad hoc nature of the RC flight control limited the resolution and breadth of their results. Mallon et al. [10] utilized a quadrotor platform and obtained a slightly improved resolution of measurements through the use of two anemometers onboard the UAV. However, they were only able to obtain measurements directly behind the ship, unable to traverse into the free-stream region of air flow due to the difficulty of maintaining stability with RC control. Gamagedara et al. [11] improved on this design by adding a camera to the ship deck, performing optical flow to improve the relative state estimation of the UAV. While the spatial association of air wake measurements was improved, the approach still suffered from the same stability issues with RC flight and the flight envelope was also limited to a very small region of air wake measurement. Kumar et al. [12] have provided the most spatially extensive set of air wake measurements with a small RC helicopter that uses an artificial neural network to associate measured angular rate disturbances on the vehicle with the turbulent component of air wake velocities. However, their platform requires a significant vehicle-specific calibration process to train their neural network and is unable to measure the steady-state velocity component of the air wake. Further, the employment of an artificial neural network, crucial to their air wake measurement process, represents a black box whose results are difficult to verify in the presence of unfamiliar vehicle flight behavior or confounding RC pilot inputs.

We present an unmanned air system (UAS) for in-situ air wake measurement that is capable of providing high-resolution measurements of both turbulent and steady-state flow with a spatial breadth sufficient to characterize a significant portion of the ship air wake profile. This task is accomplished through a novel flight control configuration where a small UAV flies autonomously while attached to the end of a tether, resulting in stable flight trajectories capable of entering the free stream region of the ship air wake. State feedback control for the UAV is afforded through the use of a standard nonlinear state estimator. Precise relative state estimates between the ship deck and UAV are obtained via a separate relative state estimator that fuses differential GPS and vision-based pose measurements from active infrared (IR) beacons mounted on the ship deck. The vision-based pose measurement system, in line with recent efforts to achieve reliable relative navigation using active features in mobile environments [13, 14], is one of the primary facilitators of an accurate and robust relative estimation scheme that functions in a variety of weather conditions and at a

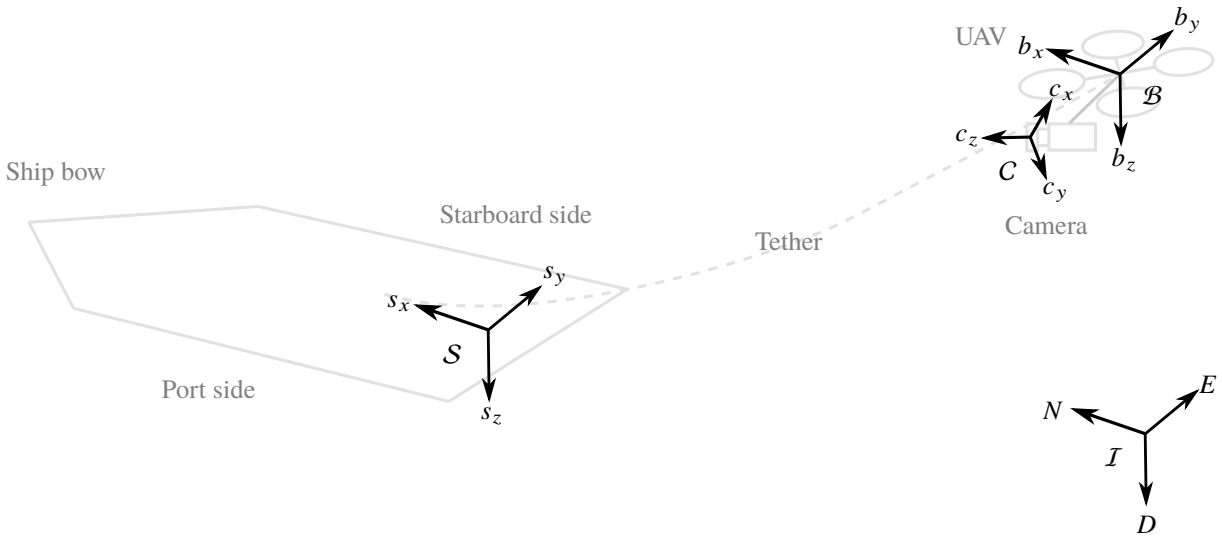

Fig. 1 Problem formulation for the UAV-based ship air wake measurement task. Principal frames and associated hardware components are marked for clarity.

large range of distances from the ship deck.

Our contributions are stated as follows:

- Present a novel tethered flight control strategy for autonomous flight capable of full space coverage of the air wake region behind a moving naval vessel at significant relative wind speeds.
- Present an accurate and robust relative state estimation scheme based on the sensor fusion of vision-based pose measurements with active IR beacons and differential GPS.
- Demonstrate the robustness of the proposed autonomous control and state estimation strategies to high wind levels and sensor noise in a high-fidelity simulation environment.

Sections I and III provide context for the presented control and estimation algorithms by introducing relevant mathematical quantities and the problem geometry. Section IV provides relevant details for each of the algorithms and hardware components of the UAS necessary for successful air wake measurement acquisition. Section V describes the high-fidelity simulation environment used to produce the preliminary results given in Section VI, followed by a corresponding analysis and plan for future hardware testing.

III. Problem Formulation

Figure 1 shows the various reference frames used in the UAS control, estimation, and measurement subsystems, as well as a simple illustration of the flight scheme. The UAV is tethered to the ship deck with a line with controllable length, maintaining the aircraft within a finite range of the moving vessel. The ship frame, denoted $\mathcal{S}$, has its origin fixed to the ship deck. The inertial North-East-Down (NED) frame is denoted as $\mathcal{I}$. The $\mathcal{S}$ and $\mathcal{I}$ frames differ in orientation only by a yaw angle, assuming no significant heaving by the ship. The UAV body frame $\mathcal{B}$ is defined as having its origin fixed to the aircraft center-of-mass (COM) with the x-axis b_x coming out the front of the aircraft, the y-axis b_y pointing to the right, and the z-axis b_z pointing down. Velocities, forces, and torques are generally expressed in $\mathcal{B}$, whereas positions are either expressed in $\mathcal{S}$ or $\mathcal{I}$. The UAV camera frame C is rigidly mounted to $\mathcal{B}$ with its z-axis c_z pointed straight out of the camera lens, its x-axis c_x pointed to the right, and its y-axis c_y pointed down.

In this work, there are two types of states referenced: an absolute state ${}^{\mathcal{I}}\boldsymbol{x}$ and a relative state ${}^{\mathcal{S}}\boldsymbol{x}$. While the exact components of the absolute and relative states in the context of filtering are explained in Section IV.C, the absolute state refers to the state of $\mathcal{B}$ relative to the inertial frame $\mathcal{I}$ and the relative state also refers to the state of $\mathcal{B}$, but this time relative to $\mathcal{S}$. The absolute state is used primarily for UAV flight control and the relative state is used primarily for giving spatial context to the obtained air wake velocity measurements.

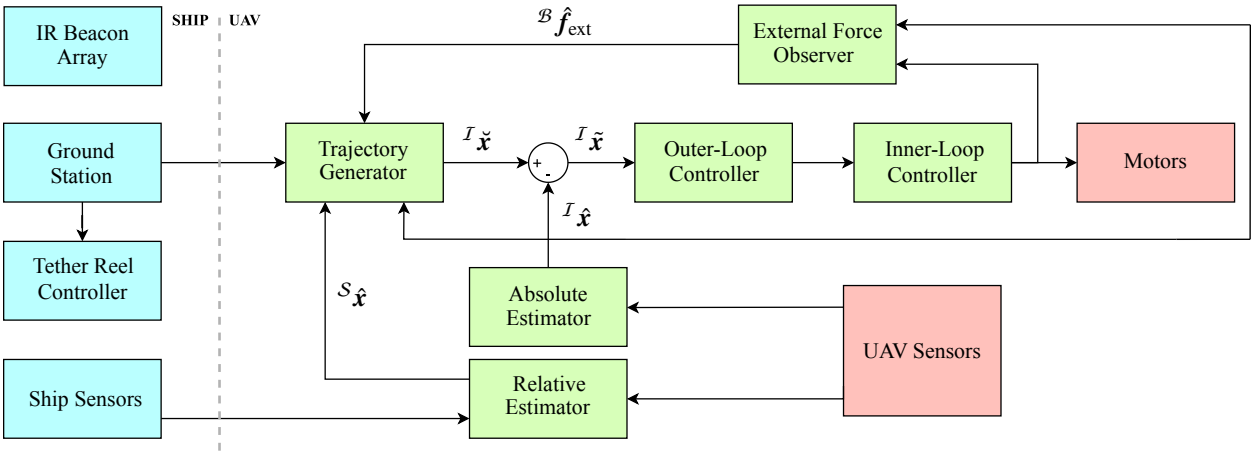

Fig. 2 Autonomous flight control system architecture, demarcating systems present onboard the UAV during flight versus systems which remain on the ship deck. UAV plant components are colored red, UAV flight control components are colored green, and components mounted on the ship are colored blue.

IV. System Overview

Figure 2 provides a high-level overview of the system architecture, including the major hardware and software components both onboard the ship deck and onboard the UAV. Communication between the ship and the UAV is facilitated with a set of WiFi antennas, and all algorithms pertaining to autonomous control and state estimation are implemented with the Robot Operating System (ROS) [15] and run on an ODROID XU-4 computer onboard the UAV for robustness in the event of connection dropout. A tether reel controller box and user-operated ground station computer reside on the ship deck, providing the software and hardware links to command the aircraft from the ship. Sensors are present both on the ship as well as onboard the aircraft to aid in both inertial-frame and relative-frame navigation, as explained in detail in Section IV.C. Additional context is provided by Fig. 3a, which shows the UAV measurement platform, and Fig. 3b, which depicts both the tether reel control box and the IR beacon array in their intended placement on the deck.

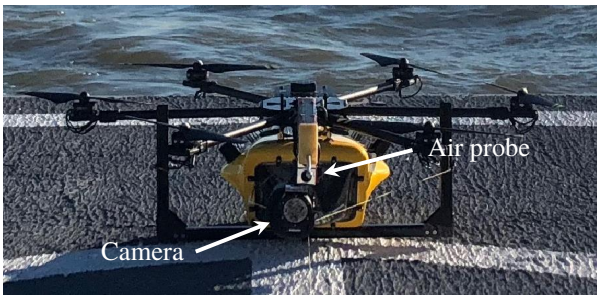

(a) UAV platform with attached sensors. The onboard computer and flight control board are housed inside a protective water-proof case, and the camera is likewise shielded from environmental or water damage.

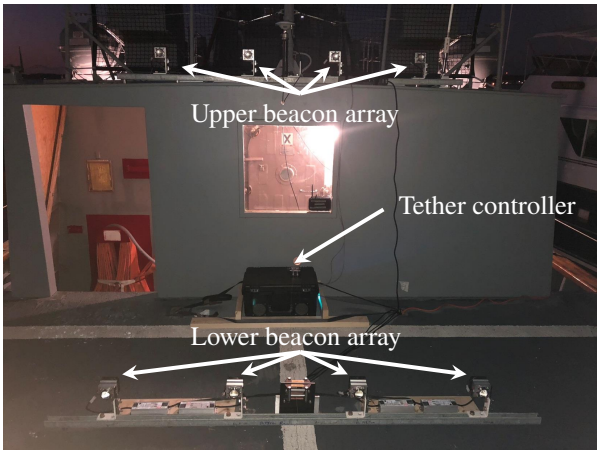

(b) UAS hardware present on ship deck during air wake measurement flights.

Fig. 3 Hardware components for the ship air wake measurement UAS.

Sections IV.A-IV.D detail the relevant design aspects for the control, estimation, and measurement subsystems, explaining how they have been tailored for the specific task of reliable high-resolution air wake measurement behind a

moving naval vessel.

A. Tethered Flight Control

One of the distinguishing characteristics of this work is the fact that the UAV completes the entirety of its mission autonomously. The automated nature of the flight control and corresponding commanded flight trajectories adds an element of systematic regularity and repeatability to the experiment. Additionally, the autonomous flight control removes the need to account for idiosyncrasies of a remote pilot when assessing the level of bias in the measurements. Referencing Fig. 2, the autonomous flight software for the UAV consists of the ground station and tether reel controller on the ship and external force observer, trajectory generator, outer-loop controller, and inner-loop autopilot onboard the aircraft. The high-level functionality of each component can be summarized as:

- The *ground station* allows a user on the ship to interface with the UAV remotely via a WiFi connection and send commands such as takeoff, land, maintain altitude, collect data, etc.
- The *tether reel controller* uses a tension sensor to alter the length of the tether as commanded by the ground station in such a way as to prevent the tether tension from varying widely and causing too much slack with feedback control.
- The *external force observer* uses the current absolute state estimate and motor commands to estimate the aggregate external force acting on the UAV in real time. From this estimate, the level of tether tautness can be deduced under nominal conditions, as explained below.
- The *trajectory generator* listens to commands from the ground station and to estimates of the current absolute state, relative state, and external force. It generates reference velocity and altitude commands for the outer-loop controller.
- The *outer-loop controller* uses proportional-integral-derivative (PID) control loops to generate reference attitude and yaw rate commands for the inner-loop autopilot.
- The *inner-loop autopilot* performs attitude control, also with PID, to generate motor PWM commands.

After takeoff, the UAV flies into the air wake flow region over the water and behind the ship, orienting itself so that its x-axis b_x, coinciding with its front, is pointed directly at the origin of $\mathcal{S}$. Once it has reached this state, system enters the air wake measurement phase, with the air probe sampling air velocities at 70 Hz.

The interplay between the external force observer, trajectory generator, and outer-loop controller during the air wake measurement phase requires further discussion to shed some light on the unique aspects of the control strategy for the proposed system. During the air wake measurement phase, the trajectory generator proceeds to command velocities aligned with the y-axis b_y of the UAV body frame at discrete altitudes so that the air probe can collect data at points on semi-circular arcs, as shown in Fig. 4. By commanding various tether lengths and altitudes, a cylindrical grid of air wake measurements is amassed. Tracking body-frame lateral velocities with the outer-loop controller instead of position commands in the inertial frame simplifies the controller objective and avoids integrator wind-up issues that would arise from attempting to arrive at a point in inertial space rendered unreachable by the tether constraint. However, it is also necessary for the tether to be taut in order for lateral velocity commands to result in the desired semi-circular arc trajectories. Tether tautness has the additional desirable effect of driving the aircraft to be constantly yawed towards the tether anchor point, effectively passively stabilizing the longitudinal and yaw dynamics.

Because tether tautness is so important to the effectiveness of the air wake measurement phase control strategy, the trajectory generator is also constantly monitoring the output of the external force observer during this phase to determine whether or not the tether is taut. Tether tautness is determined using the binary criterion of comparing the component of ${}^{\mathcal{B}}\hat{\boldsymbol{f}}_{\text{ext}}$ aligned with b_x against a certain threshold value, ${}^{\mathcal{B}}f_{\text{ext,thresh}}$. The observer is an UKF proposed by [16] to deduce the generalized external forces acting on a small UAV given the motor speed commands ω_i and estimated state. The UKF model for translational dynamics is given by

$$ {}^{\mathcal{B}}\dot{\boldsymbol{v}}_{\mathcal{B}/\mathcal{I}} = \frac{1}{m}\left({}^{\mathcal{B}}\boldsymbol{f}_{\text{ext}} + \begin{bmatrix} 0 \\ 0 \\ {}^{\mathcal{B}}f_{\text{thrust}} \end{bmatrix} + {}^{\mathcal{B}}\boldsymbol{f}_{\text{aero}} \right) - R(\boldsymbol{q}_{\mathcal{I}}^{\mathcal{B}}) \begin{bmatrix} 0 \\ 0 \\ g \end{bmatrix}. \tag{1} $$

The corresponding aerodynamic model

$$ {}^{\mathcal{B}}\boldsymbol{f}_{\text{aero}} = \mu \sum_{i=1}^{N} |\omega_i| {}^{\mathcal{B}}\boldsymbol{v}_{\mathcal{B}/\mathcal{I}}, \tag{2} $$

which is a function of individual rotor speeds ω_i over N rotors and linear drag constant μ, allows the filter to distinguish

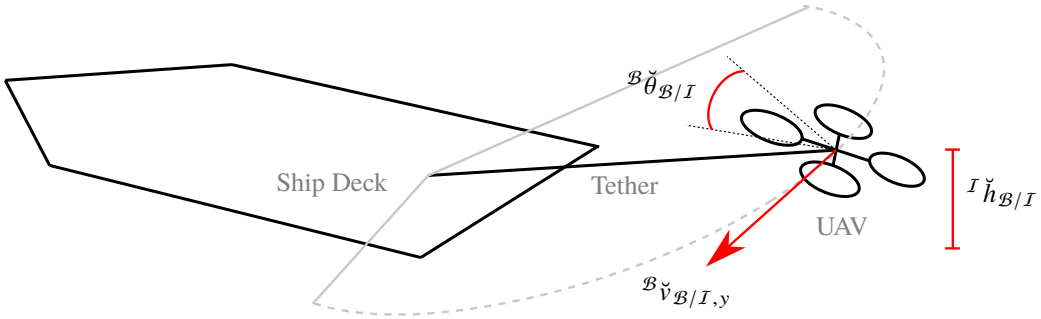

Fig. 4 Illustration of commanded states passed to the outer-loop controller: UAV pitch angle ($^{\mathcal{B}}\breve{\theta}_{\mathcal{B}/\mathcal{I}} \geq 0$), altitude ($^{\mathcal{I}}\breve{h}_{\mathcal{B}/\mathcal{I}}$), and lateral velocity ($^{\mathcal{B}}\breve{v}_{\mathcal{B}/\mathcal{I},y}$). With a taut tether, commands of this form result in semi-circular sweeping trajectories behind the moving ship.

between aerodynamic and non-aerodynamic (e.g., tether) forces assuming zero wind velocity. However, in an air wake measurement scenario where relative wind velocities are commonly in the vicinity of 6-7 m/s, the UKF filter output $^{\mathcal{B}}\hat{\boldsymbol{f}}_{\text{ext}}$ invariably consists of forces imposed on the UAV by the tether as well as coupled aerodynamic drag effects.

The consequence of the inability of the UKF to distinguish between tether and aerodynamic forces is that an effort must be made to actively fly against the tether. This is because during flight, the tether and aerodynamic forces from a relative head wind are never aligned and, in fact, are normally acting in opposing directions. Thus, actively pulling against the tether will result in a taut tether force far outweighing the magnitude of the aerodynamic forces, such that it will be easy to distinguish between a taut and slacked tether by monitoring $^{\mathcal{B}}\hat{\boldsymbol{f}}_{\text{ext}}$. To pull against the tether, the trajectory generator commands a positive pitch angle, saturated at 15 degrees, throughout the air wake measurement phase. At that level of pitch, the tether force is easily distinguishable from aerodynamic forces under almost any wind condition. The only exception arises when there is a non-negligible tailwind that actually pushes the UAV back towards the ship. The significant tailwind scenario is rare, known mostly to happen when there is a strong recirculation effect close to the stern of the ship, and can be compensated for with an intervention from a safety pilot if necessary. When the trajectory generator detects a significant, sustained tether force indicative of tether tautness, then it allows the semi-circular sweeping trajectory to continue.

Note that, while both relative and absolute state estimates are available in real-time, outer-loop control is performed off of the absolute state only for reasons explained in Section IV.C. The relative state is leveraged in the trajectory generator as it is useful for operations such as takeoff, landing, and avoiding flying too close to the ship during the air wake measurement phase. Inner-loop attitude stabilization and control for the aircraft is handled by the onboard autopilot, which sits on a dedicated flight control board. The ROSflight autopilot [17] was chosen for this platform because of its lightweight and configurable code architecture, as well as its built-in compatibility with ROS.

B. Active IR Beacon Array

To add robustness and accuracy to the real-time relative pose estimation between the $\mathcal{S}$ and $\mathcal{B}$ frames, a monocular pose estimation algorithm with active IR beacons based on [18] and [19] is employed. Pictured in Fig. 3b, two co-linear arrays of 45-watt IR beacons mounted to a light frame are fixed to the ship deck, and the position of each beacon $^{\mathcal{S}}\boldsymbol{p}_i$ expressed in frame $\mathcal{S}$ is recorded. During flight, a monocular IR camera onboard the UAV records video of the array, producing images such as the one depicted in Fig. 5a at 10 Hz. The size and brightness of the beacons afford them visibility during a bright, sunny day at distances well beyond 150 meters. During the air wake measurement process, the beacons are the brightest objects captured by the IR camera, making them ideal visual features for relative pose extraction. The captured camera images are passed through a filter to isolate the beacon features in the image plane and to reject any outlier features that do not conform to the co-linear beacon geometry. Figure 5b shows a filtered (and cropped) version of the image taken in Fig. 5a at a distance of 150 meters.

The filtered image features are subsequently associated with the pre-recorded beacon positions $^{\mathcal{S}}\boldsymbol{p}_i$ to create eight 3D-to-2D point correspondences, leveraging the knowledge that the UAV will always be viewing the beacon array from an upright and forward-facing position. These point correspondences are used together with the previously known camera intrinsic parameters to deduce the 6-degree-of-freedom (6-DOF) transform between the ship frame $\mathcal{S}$ and

(a) Image captured from UAV camera of IR beacon array at a distance of 150 meters on a sunny day.

(b) Filtered camera image with programmatically isolated beacon feature points in the image plane.

Fig. 5 Vision-based relative pose measurement system using active IR beacon features. Images obtained from [20].

the camera frame $\mathcal{C}$ using a Perspective-n-Point algorithm run in conjunction with RANSAC for outlier detection. The Perspective-n-Point algorithm uses a nonlinear optimization routine to minimize the re-projection error of each feature point correspondence by using the 6-DOF relative pose as the design variable. The transform between the UAV body frame $\mathcal{B}$ and the camera frame $\mathcal{C}$, assumed to be known, is then used to obtain the vision-based relative pose measurement from $\mathcal{S}$ to $\mathcal{B}$. The pose extraction algorithm, tailored to the two-row beacon array, is able to match the input image rate at a speed of 10 Hz while running on the onboard computer.

Using a 1:35 scale model of the IR beacon array and a Vicon motion capture system, the error of the vision pose measurement system in hardware is found to be less than 2° in orientation and 5 cm in translation. However, due to the nature of nonlinear optimization and possible image distortion that can occur with accelerations during flight, the vision system also has a final outlier detector to reject solutions which suggest that the solver has not handled a correspondence ambiguity correctly.

C. Absolute and Relative State Estimators

Two separate state estimators are run in parallel during flight: an absolute state estimator and a relative state estimator. The absolute state estimator is used for robust UAV flight control and the relative state estimator is primarily for facilitating accurate spatial characterization of measured air wake velocities. In essence, the absolute estimator tracks the UAV pose with respect to the inertial frame, whereas the relative estimator tracks the UAV pose with respect to the moving ship frame. Both estimators estimate the UAV velocity with respect to the inertial frame, but the relative estimator also estimates the inertial velocity of the ship and passive rotation of the ship frame w.r.t. the inertial frame, which allows the estimated UAV inertial velocity to contribute to the dynamics of the relative UAV pose. Both estimators observe IMU and barometer biases. The absolute and relative states can be expressed as Eq. 3 and Eq. 4, respectively.

$$
{}^{\mathcal{I}}\boldsymbol{x} \triangleq \begin{bmatrix} {}^{\mathcal{I}}\boldsymbol{p}_{\mathcal{B}/\mathcal{I}} & \boldsymbol{q}_{\mathcal{I}}^{\mathcal{B}} & {}^{\mathcal{B}}\boldsymbol{v}_{\mathcal{B}/\mathcal{I}} & \boldsymbol{\beta}_a & \boldsymbol{\beta}_\omega & \beta_b \end{bmatrix}^T \in \mathbb{R}^{13} \times \mathbb{S}^3 \tag{3}
$$

$$
{}^{\mathcal{S}}\boldsymbol{x} \triangleq \begin{bmatrix} {}^{\mathcal{S}}\boldsymbol{p}_{\mathcal{B}/\mathcal{S}} & \boldsymbol{q}_{\mathcal{S}}^{\mathcal{B}} & {}^{\mathcal{B}}\boldsymbol{v}_{\mathcal{B}/\mathcal{I}} & \boldsymbol{\beta}_a & \boldsymbol{\beta}_\omega & \beta_b & \boldsymbol{q}_{\mathcal{I}}^{\mathcal{S}} & {}^{\mathcal{I}}\boldsymbol{v}_{\mathcal{S}/\mathcal{I}} \end{bmatrix}^T \in \mathbb{R}^{16} \times \mathbb{S}^3 \times \mathbb{S}^3 \tag{4}
$$

For both the absolute and relative case, estimation is performed with the indirect (or “error-state") form of the extended Kalman filter (EKF), referred to as the error-state Kalman filter (ESKF). The ESKF formulation is useful because it decomposes a state estimate $\hat{\boldsymbol{x}}$ into two components: a nominal state term $\boldsymbol{x}$ and an error-state term $\tilde{\boldsymbol{x}}$ such that $\hat{\boldsymbol{x}} \triangleq \boldsymbol{x} + \tilde{\boldsymbol{x}}$. Whereas the dynamics of the nominal state are fast with possibly highly nonlinear terms, the dynamics of the error-state are comparatively slow and are much better approximated as linear. Thus, because the ESKF propagates the nominal state directly through integration and only treats the error-state as a stochastic process subject to innovation corrections, its numerical properties are generally more desirable than its direct counterpart. Moreover, when $\hat{\boldsymbol{x}}$ also

contains a component that cannot be expressed as a vector (such as attitude), the ESKF has the additional advantage of having all of its vector operations performed in manifold tangent spaces. When the state estimate contains a nonlinear manifold component, the definition of $\hat{\boldsymbol{x}}$ should be augmented to $\hat{\boldsymbol{x}} \triangleq \boldsymbol{x} \boxplus \tilde{\boldsymbol{x}}$, where $\boxplus$ is the operator that increments members of a manifold (to the left of the operator) with a vector term belonging to a vector space tangent to the manifold (to the right of the operator) [21].

The principal difference between the ESKF and the EKF is the need to derive the error-state dynamics and their corresponding Jacobians on the manifold. For the absolute ESKF, the error-state dynamics are given by

$$
\begin{aligned}
{}^{\mathcal{I}}\dot{\tilde{\boldsymbol{p}}}_{\mathcal{B}/\mathcal{I}} &= R^{-1}(\boldsymbol{q}_{\mathcal{I}}^{\mathcal{B}} \boxplus \tilde{\boldsymbol{q}}_{\mathcal{I}}^{\mathcal{B}})({}^{\mathcal{B}}\boldsymbol{v}_{\mathcal{B}/\mathcal{I}} + {}^{\mathcal{B}}\tilde{\boldsymbol{v}}_{\mathcal{B}/\mathcal{I}}) - R^{-1}(\boldsymbol{q}_{\mathcal{I}}^{\mathcal{B}})\,{}^{\mathcal{B}}\boldsymbol{v}_{\mathcal{B}/\mathcal{I}} && (5)\\
\dot{\tilde{\boldsymbol{q}}}_{\mathcal{I}}^{\mathcal{B}} &= \boldsymbol{\omega}_m - \boldsymbol{\beta}_\omega + \boldsymbol{\eta}_\omega - \tilde{\boldsymbol{\beta}}_\omega - R(\boldsymbol{q}_{\mathcal{I}}^{\mathcal{B}} \boxplus \tilde{\boldsymbol{q}}_{\mathcal{I}}^{\mathcal{B}})R^{-1}(\boldsymbol{q}_{\mathcal{I}}^{\mathcal{B}})(\boldsymbol{\omega}_m - \boldsymbol{\beta}_\omega) && (6)\\
{}^{\mathcal{B}}\dot{\tilde{\boldsymbol{v}}}_{\mathcal{B}/\mathcal{I}} &= R(\boldsymbol{q}_{\mathcal{I}}^{\mathcal{B}} \boxplus \tilde{\boldsymbol{q}}_{\mathcal{I}}^{\mathcal{B}})\begin{bmatrix}0\\0\\g\end{bmatrix} + \boldsymbol{a}_m - \boldsymbol{\beta}_a + \boldsymbol{\eta}_a - \tilde{\boldsymbol{\beta}}_a - \left[\boldsymbol{\omega}_m - \boldsymbol{\beta}_\omega + \boldsymbol{\eta}_\omega - \tilde{\boldsymbol{\beta}}_\omega\right]_\times ({}^{\mathcal{B}}\boldsymbol{v}_{\mathcal{B}/\mathcal{I}} + {}^{\mathcal{B}}\tilde{\boldsymbol{v}}_{\mathcal{B}/\mathcal{I}})\\
&\quad - \left(R(\boldsymbol{q}_{\mathcal{I}}^{\mathcal{B}})\begin{bmatrix}0\\0\\g\end{bmatrix} + \boldsymbol{a}_m - \boldsymbol{\beta}_a - [\boldsymbol{\omega}_m - \boldsymbol{\beta}_\omega]_\times^{\mathcal{B}}\boldsymbol{v}_{\mathcal{B}/\mathcal{I}}\right), && (7)
\end{aligned}
$$

with all other error-state component time derivatives set to zero. The error-state dynamics for the relative ESKF take an analogous form, assuming that $\boldsymbol{q}_{\mathcal{S}}^{\mathcal{B}}$ and ${}^{\mathcal{I}}\boldsymbol{v}_{\mathcal{S}/\mathcal{I}}$ are both quasi-static quantities.

The filter propagation and update steps are defined by slight modifications to the standard EKF equations, which are

$$
\begin{aligned}
\Phi_k &= \frac{\partial}{\partial \boldsymbol{x}} f_k(\boldsymbol{x}, \boldsymbol{u}_k)|_{\boldsymbol{x}=\hat{\boldsymbol{x}}_k^+} && (8)\\
\hat{\boldsymbol{x}}_{k+1}^- &= f_k(\hat{\boldsymbol{x}}_k^+, \boldsymbol{u}_k) && (9)\\
Q_{k+1}^- &= \Phi_k Q_k^+ \Phi_k^T + W_k && (10)\\
\boldsymbol{r}_k &= \boldsymbol{y}_k - h(\hat{\boldsymbol{x}}_k^-) && (11)\\
C_k &= \frac{\partial}{\partial \boldsymbol{x}} h(\boldsymbol{x})|_{\boldsymbol{x}=\hat{\boldsymbol{x}}_k^+} && (12)\\
S_k &= V_k + C_k Q_k^- C_k^T && (13)\\
Q_k^+ &= Q_k^- - Q_k^- C_k^T S_k^{-1} C_k Q_k^- && (14)\\
L_k &= Q_k^- C_k^T S_k^{-1} && (15)\\
\hat{\boldsymbol{x}}_k^+ &= \hat{\boldsymbol{x}}_k^- + L_k \boldsymbol{r}_k, && (16)
\end{aligned}
$$

with $\boldsymbol{u}_k = \begin{bmatrix}\boldsymbol{a}_m & \boldsymbol{\omega}_m\end{bmatrix}^T$ as the current IMU accelerometer and gyro measurements. At each propagation step, Eq. 5-7 are linearized about the current nominal state and discretized with first-order Euler integration to obtain Φ_k with Eq. 8. After each update step, the error-state mean is injected into the nominal state and subsequently reset to zero with a corresponding filter covariance reset. To add robustness to outlier measurements, covariance gating [22] is also implemented for each measurement update.

The absolute estimator fuses only standard sensors onboard the UAV, including an IMU, GPS, and barometer, with the exception of vision-based attitude corrections when the IR beacon array is in view of the onboard camera. These attitude corrections allow the IMU accelerometer and gyro biases to be observable, which is important because low-cost IMU measurements (particularly gyro measurements) can drift significantly over the course of several minutes. IMU bias observability requires inertial attitude updates. Moreover, though the vision-based attitude measurement gives $\boldsymbol{q}_{\mathcal{S}}^{\mathcal{B}}$ and not $\boldsymbol{q}_{\mathcal{I}}^{\mathcal{B}}$, this fact does not compromise the stability of the estimator assuming that the ship frame does not heave significantly for sustained periods of time.

The relative estimator, by contrast, fuses the IMU, barometer, differential GPS, full vision-based pose measurement, and a separate GPS unit mounted on the ship deck. The ship-mounted GPS provides information about the ship frame velocity and also allows for real-time kinematic (RTK) differential GPS calculations between the ship and the UAV. Because differential GPS gives relative position in the inertial frame, disparities between its and the vision pose calculator's relative position measurements informs the estimation of $\boldsymbol{q}_{\mathcal{I}}^{\mathcal{S}}$. This property of iteratively estimating the

Table 1 Wind tunnel validation results for the omnidirectional air probe.

Quantity	True Value	Lower Measurement Error Bound %	Upper Measurement Error Bound %
Velocity (m/s)	5	-5	5
	10	-10	5
	15	-10	10
Angle of Attack (°)	-45	-8	8
	0	-2	10
	45	-5	5
Side Slip Angle (°)	-45	-2	3
	0	-4	5
	45	0	4

passive rotation between the inertial and ship frames, however, exhibits a transient behavior that can adversely affect the accuracy of the estimated UAV velocity when the IR beacon array comes into the view of the onboard camera for the first time. Though the velocity estimates quickly re-converge within a matter of seconds, the effect is significant enough to merit controlling the UAV off of the absolute estimated state alone while using the relative estimated state in real-time only for high-level trajectory generation logic based only on relative positions.

D. Omnidirectional Air Probe

Air wake velocity measurement is performed by an omnidirectional anemometer air probe that is mounted on the front of the UAV (see Fig. 3a). The probe has a rated airspeed range of 5 to 50 meters per second and logging rate of up to 70 Hz, allowing for high spatial resolution of air wake measurements in-flight. For a successful three-dimensional characterization of the measured airspeed vector at each location, the probe must be able to report the velocity, angle of attack, and side slip angle to sufficient accuracy. Extensive wind tunnel testing has been performed to validate the accuracy of the wind probe at various velocities, angles of attack, and side slip angles. Table 1 reports the accuracy ranges of the wind tunnel measurement trials for a representative range of wind conditions.

With all measurements bounded within ±10%, the air probe is well-suited for calculating both the turbulent and steady-state components of the air wake velocity profile in three dimensions.

V. Simulation Environment

The use of an autonomous control strategy coupled with real-time sensor fusion in-the-loop necessitates a high-fidelity test bed for development and validation of the flight-critical algorithms. To partially fulfill this need, a simulator built in ROS has been developed to model the 6-DOF UAV dynamics, ship motion, tether contact dynamics, sensor noise models, and aerodynamic drag effects present in a mobile, maritime environment with significant wind. Figure 6 shows sample views of the simulation environment, depicting the naval vessel, UAV, and tether. The simulator runs all onboard algorithms described in Figure 2 as hardware-in-the-loop (HIL) with the UAV ODROID computer and runs through all phases of the air wake measurement process, including takeoff, measurement acquisition, return-to-home, and land. An identical ground station interface to the one used in field testing is also provided for the user to practice sending commands to the UAV and tether reel controller.

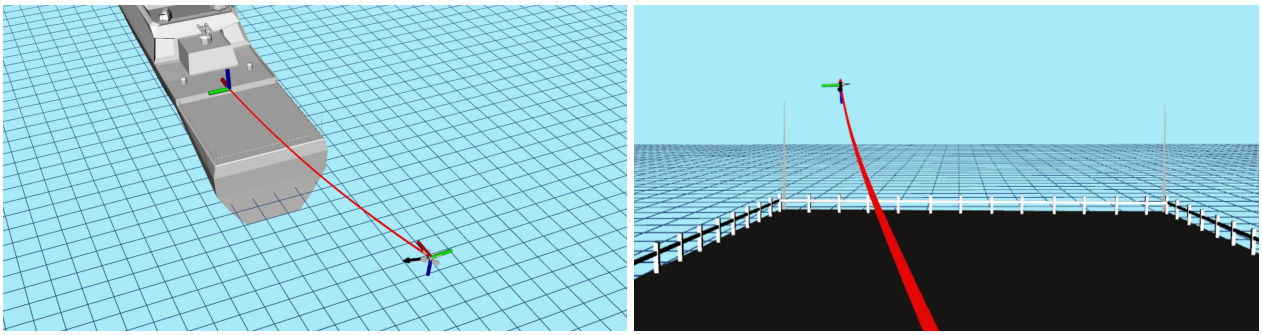

Fig. 6 Simulation environment for the air wake measurement system, used for testing all phases of the measurement flight in the presence of configurable wind disturbances and at varying levels of sensor noise and bias. The simulated tether line, colored red, keeps the airborne UAV anchored to a naval vessel moving forward at a steady velocity.

Environmental wind conditions are simulated using a Dryden gust stochastic process model. At non-negligible relative wind speeds, aerodynamic effects begin to impose significant moment and force disturbances on small aircraft. These effects are modeled in the simulator through the environmental implementation of the rotor blade flapping effect [23], which occurs due to both linear drag on the aircraft frame as well as differential moments that arise across the individual rotors when the half of the rotor blade moving into the wind generates more lift than the half moving with the wind. For example, in the scenario where the UAV is flying directly behind the ship and facing the air wake stream, a significant differential moment is generated about the UAV pitch axis, described by

$$^{\mathcal{B}}M_y = \sum_{i}^{N} (f_{i,\text{thrust}} h_i \sin(k_f v_{\text{wind},b_x}) + k_\beta k_f v_{\text{wind},b_x}), \tag{17}$$

where v_{wind,b_x} is the component of relative wind velocity aligned with the UAV body-x-axis and h_i is the height of rotor blade i with respect to the UAV COM, summed over N rotor blades. With a relative headwind, the rotor blade flapping effect generates a positive moment about the pitch axis, resulting in a steady-state pitch disturbance through the duration of the flight. The effects are not limited to moments about the pitch axis, and must be reckoned with in a robust tethered flight control strategy. Tether forces are modeled using the geometry of a catenary curve with spring-like contact dynamics, following the approach outlined in [24].

All ship-based and UAV sensors involved in both absolute and relative state estimation are implemented with noise and random walk bias levels commensurate with empirically gathered data. The input sensor data, consisting of the IMU, barometer, camera, and GPS modules are modeled with added Gaussian white noise. The GPS measurements from the modules on the ship and onboard the UAV are modeled as Gauss-Markov processes, following the strategy of [25] to model GPS error from ephemeris data, satellite clock, ionosphere, and troposphere-related effects.

To establish the simulation environment as a useful measure of UAS suitability for ship air wake measurement, the parameters defining UAV dynamic characteristics and aerodynamic susceptibility are validated against measured behavior in hardware. The UAV motor parameters are measured directly using the Dynamometer Series 1580 thrust stand, mass is measured on a scale, and aerodynamic parameters for the rotor blade flapping effect are estimated using least-squares optimization with hardware data from several motion capture flights. Sensor noise and bias parameters are validated against recorded sensor data on the hardware platform. As a final validation test, the simulated UAV has been found to exhibit the same qualitative flight behavior as the hardware platform as measured with a motion capture system when provided identical inputs to the inner-loop autopilot. With validated dynamic behavior, the simulation environment provides a suitable test bed for evaluating control and estimation algorithm performance before executing a mission on an actual naval vessel.

VI. Simulation Results

In preparation for UAS testing onboard a naval vessel in a maritime environment, results are provided that validate the performance of the absolute state estimator, the relative state estimator, and the autonomous control strategy in a simulated windy environment with implemented sensor noise and bias. Specifically, the results in this section correspond

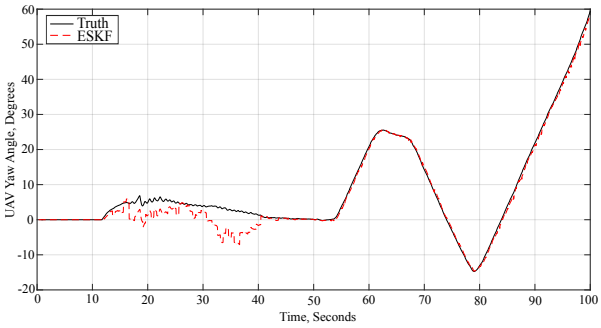

Fig. 7 Absolute state estimate of UAV yaw with respect to the inertial frame over the course of a simulated ship air wake measurement flight. Attitude corrections in the estimate are activated once the IR beacon array comes into view 40 s into the simulation.

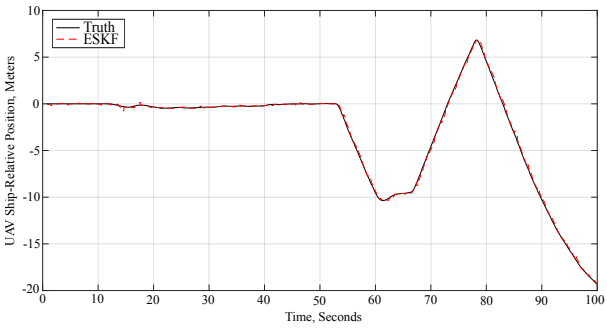

Fig. 8 Relative state estimate of UAV y position w.r.t. and expressed in $\mathcal{S}$ over the course of a simulated ship air wake measurement flight. Accurate relative state position estimation is facilitated by the fusion of differential GPS and, after 40 s into the simulation, vision-based pose measurements.

to simulation tests run in an environment with relative headwind speeds in the vicinity of 10 meters per second, which is in the upper range of expected average relative wind speeds to be experienced during tethered flight. The simulated flights from which these results are extracted carry out the tasks of takeoff, establishing tether tension, and sweeping behind a moving ship at a commanded altitude, exciting all of the different flight modes of the UAV for trajectory tracking performance evaluation.

The performance of the absolute state estimator is evaluated on the basis of how well the states used in the flight control feedback loop conform to the true state values provided by the simulator. These feedback states consist the UAV altitude, translational velocities, attitude, and angular rates.

Both outdoor and simulation testing demonstrates that while GPS provides less drift-prone velocity than position estimates, the barometer provides sufficient, albeit noisy, altitude stability to ensure that the absolute altitude estimate does not drift beyond approximately one meter from the true altitude. A similar effect, well-documented in small UAV applications, occurs with the UAV attitude as the IMU gyro biases are corrected by the less drift-prone accelerometer measurements. The attitude component most susceptible to drift over very short time scales is the yaw angle, which relies principally on gyro signal integration in the absence of corrective vision-based attitude measurements from the IR beacon array. Figure 7 demonstrates the amount of drift exhibited by the yaw angle estimate until the IR beacon array comes into full view of the onboard camera 40 seconds into the simulation, subsequently providing very precise attitude estimates. Moreover, it is important to note that while no active yaw control is employed in the flight control scheme, a comparison between Fig. 7 and 8 reveals the passive yaw control effect of a taut tether, which maintains the UAV pointing towards the ship deck.

The performance of the relative state estimator is based principally on the accuracy of the estimated relative pose. Accurate estimated velocity states are also important for propagating the pose state in the event of differential GPS or vision measurement dropouts as well as compensating for relative UAV velocity when post-processing the measured wind velocity vectors. The relative estimator fuses the same sensors as the absolute estimator for velocity estimation, but with the added benefit of centimeter-level accuracy in relative position and single-degree-level accuracy in attitude from the differential GPS and vision-based pose sensors. Moreover, when the estimate of $\boldsymbol{q}_I^{\mathcal{S}}$ converges to a steady-state value after the IR beacon array comes into view, the full relative state estimate is found to be very stable and accurate, which is to be expected given the accuracy of the relative sensors. Figure 8 provides insight into both the accuracy of the relative position estimate as well as the stability and coverage of the sweeping patterns necessary for generating an informative vector field of measured air wake velocities.

With stable absolute and relative state estimates, the success of the autonomous control strategy is primarily a function of how well the controller is able to track the commanded absolute UAV pitch, lateral velocity, and altitude once the passively stabilizing effect of the tether is verified. Figure 9 demonstrates the pitch tracking performance of the control strategy at a relative wind speed of 10 meters per second. Due to the rotor blade flapping effect, the relative headwind induces a steady-state pitch disturbance of approximately seven degrees. Through testing at various wind speed levels, it is observed that the wind-induced pitch disturbance can be expected to range from zero to ten

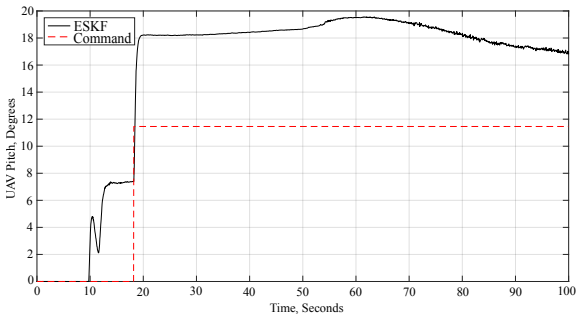

Fig. 9 UAV pitch tracking performance throughout a simulated ship air wake measurement flight. A steady-state pitch disturbance of ≈ 7° is induced by the rotor blade flapping effect at a relative wind speed of 10 m/s. Over all simulation trials, the disturbance is bounded and does not have any destabilizing effect on the flight trajectory due to the tether constraint.

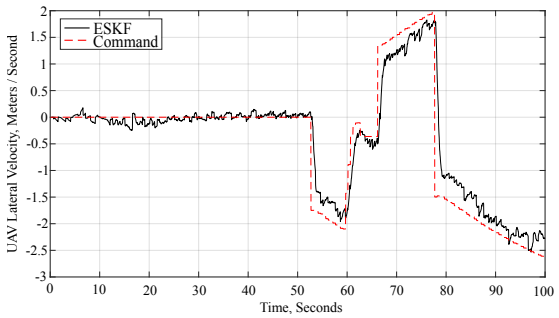

Fig. 10 UAV lateral velocity tracking performance over the course of a simulated ship air wake measurement flight. Aerodynamic drag effects are visible after 50 s, when the UAV begins to fly out from directly behind the moving ship. Despite these drag effects, velocity tracking is observed to be tractable with PID control.

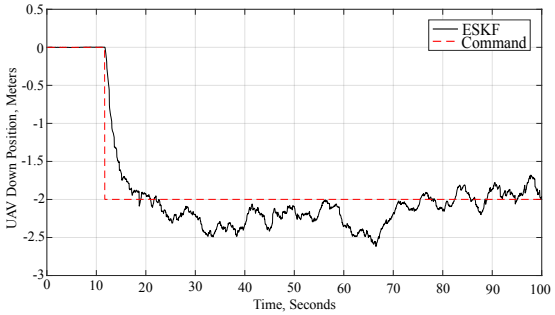

Fig. 11 UAV absolute altitude tracking performance over the course of a simulated ship air wake measurement flight. Precise absolute altitude tracking poses the greatest difficulty for the flight control system, with bounded random walk behavior about the commanded altitude due to drag and tether effects.

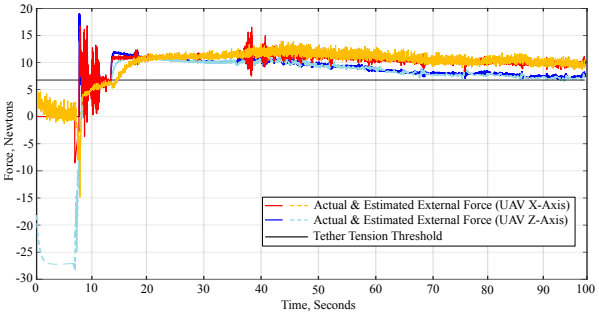

Fig. 12 Comparison between the x and z components of ${}^{\mathcal{B}}\boldsymbol{f}_{\text{ext}}$ versus ${}^{\mathcal{B}}\hat{\boldsymbol{f}}_{\text{ext}}$. The estimated forces in the UAV b_x, b_z directions reveal the takeoff point at ≈ 8 s and the point of tether tautness at ≈ 15 s. The tether tension threshold, ${}^{\mathcal{B}}f_{\text{ext,thresh}}$, is compared with the x-component of ${}^{\mathcal{B}}\hat{\boldsymbol{f}}_{\text{ext}}$ to determine tether tautness.

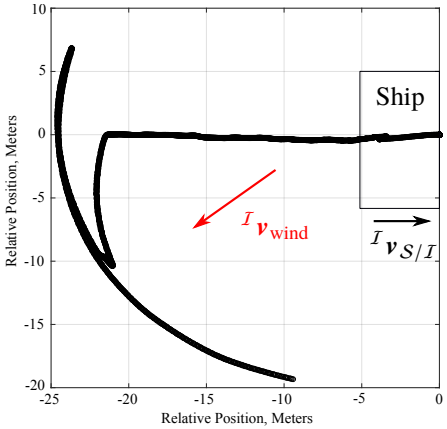

Fig. 13 Top view of a sweep trajectory from a simulated UAV flight in the presence of 10 m/s wind. Position values expressed in the $\mathcal{S}$ frame. The commanded trajectory is tailored to the principal wind direction, providing symmetric coverage about the air wake generated by the wind's interaction with the ship superstructure. In order for a symmetric sweep like the one shown, the estimated wind direction must be measured and reported to the trajectory generator before flight.

degrees. Because the pitch disturbance is bounded and has no appreciable effect on flight stability due to the ability of the tether reel controller to maintain a relatively taut tether, no attempt is made to place integral control on pitch (which can introduce low-frequency oscillations). Additionally, no effort is made to estimate the wind vector in real time for computing feed-forward pitch control.

Though integral control is avoided in most cases, it is used in lateral velocity tracking in order to achieve the desired area coverage in the face of increasing aerodynamic drag as the UAV sweep angle increases. Because the lateral velocity vector is defined to be perpendicular to the tether, the tether does not lead to integrator windup as would be the case with a longitudinal or position-based reference state command. Figure 10 demonstrates the ability of the controller to track reference lateral velocities such that the UAV is able to sweep angles up to 50-60 degrees even in the presence of heavy wind. Additionally, Fig. 13 provides a top-down view of one such sweeping trajectory, showing how the UAV is able to cover the region where air wake effects (defined by wind direction with respect to the ship superstructure) are present.

It is apparent from analyzing tracking performance that the greatest difficulty comes in tracking altitude, as shown in Fig. 11. Comparing the ESKF altitude estimate with the reference altitude command, the state exhibits a random walk centered on the commanded value. This behavior is attributable to both the rotor blade flapping effect as well as the fact that altitude controllability is weakened with a sustained non-zero aircraft pitch value. The altitude error, however, remains bounded at around half a meter over the course of all simulation trial flights with different wind speeds. This level of error is dealt with for landing operations by allowing the tether to "reel in" the aircraft in the absence of integral control on altitude.

In addition to reference state tracking, the ability to automatically deduce tether tautness is important for the trajectory generator to determine when it is feasible to begin sweeping with pitch and lateral velocity commands. For simulated testing, ${}^{\mathcal{B}}f_{\text{ext,thresh}}$ is assigned the amount of backward thrust generated with a pitch value of 10 degrees, since this would correspond to the amount of tension in a taut tether in the absence of wind and at an altitude that is level with the tether reel controller. As suggested by Fig. 12, this choice of ${}^{\mathcal{B}}f_{\text{ext,thresh}}$ leaves enough buffer to make a binary determination of tether tautness even with significant aerodynamic forces opposing the force of the tether. A close examination of the z-component of ${}^{\mathcal{B}}\hat{\boldsymbol{f}}_{\text{ext}}$ on the plot also reveals the various stages of flight, such as takeoff at 8 seconds and tether tautness at 15 seconds. The relatively large z-component of ${}^{\mathcal{B}}\hat{\boldsymbol{f}}_{\text{ext}}$ is attributable to the UAV pitch angle and the fact that the estimated external force is expressed in $\mathcal{B}$.

These results over many simulated trials with significant aerodynamic disturbances, coupled with the implementation of all relevant dynamic effects and the efforts made to validate the modeled effects against empirical motion capture data, demonstrate the suitability of the presented control and estimation strategies for the air wake measurement environment. In aggregate, the body of testing work performed to date instills confidence in the ability of the UAS to perform the allotted air wake measurement task in hardware and to corroborate these presented results in a maritime environment.

VII. Indoor Hardware Results

Hardware flight testing in a controlled indoor environment provides further validation of simulation results. Each performance indicator from the simulated tests is measured in a replicated testing scenario in hardware. In the indoor environment, motion capture software is used to evaluate tracking and state estimation accuracy, as well as spoof absolute and relative GPS sensor measurements with added bias and noise. Apart from GPS, all other sensor data come from real-time hardware. The indoor flight testing results bear striking similarity to those obtained in simulation, further validating the effectiveness of the flight control software for real-world air wake measurement missions.

The simulation environment models the UAV dynamics, tether constraint, ship motion, wind/aerodynamic effects, and a full sensor suite. The indoor testing setup is designed to replicate those conditions as closely as possible, as they are meant to be representative of the real maritime mission environment. Figure 14 shows the indoor flight testing arrangement, which consists of the UAV hardware platform and sensor suite, tether reel controller, 1:35 scale model LED beacon array, and artificial wind generators. As can be seen from the figure, reflective markers are also attached to both the UAV and beacon array so that the Vicon motion capture system is able to provide truth references for their states. These truth references are useful both for evaluating tracking and estimation performance as well as forming the basis for spoofed sensor measurements. The indoor setup is able to replicate (in miniature) the simulated and hypothetical maritime environments, as real hardware, real-time sensing, and substantial wind disturbances are used during tethered flight. In terms of real-time sensing, the following actual sensor data is used:

- Camera and corresponding relative pose estimation,
- Barometer altitude and pressure data,
- IMU accelerometer and gyro data,

and the following sensor data is spoofed from motion capture (with added noise and bias levels consistent with those described in Section V):

- Absolute GPS measurements of UAV position,
- Relative GPS measurements between the tether reel controller and UAV.

The results presented in this paper correspond to the following physical arrangement:

Table 2 Physical parameters for the presented indoor hardware flight tests.

Parameter	Value
Wind Speed (Furthest Point in Trajectory)	5±0.5 meters/second
Wind Speed (Closest Point in Trajectory)	6±0.75 meters/second
Tether Length	7 meters
Sweep Angle	40°

In total, four full flight tests, consisting of takeoff, tether tension establishment, several sweeps, and landing, have been carried out with artificial wind, with an additional four tests without wind. The results in this section present representative data indicative of the observed flight and state estimation performance over all flight trials with wind.

The relative estimator, fusing spoofed GPS and actual vision, barometer, and IMU data, achieves comparable accuracy and consistency (Fig. 15) to the relative estimator fusing purely simulated data (Fig. 8). Similarly, relative attitude estimation accuracy is comparable to simulation levels.

As with Fig. 9, Fig. 16 depicts a steady-state pitch offset induced by the 4-7 m/s wind. The offset is not present in the absence of wind, validating the simulation model for the rotor blade flapping effect. Empirically, it has been determined that sustained roll and pitch angles over 30 degrees begin to diminish the altitude control authority of the UAV. It is important to note that roll and pitch angles of that size have only been imposed artificially, and have never arisen by accident due to wind disturbances–especially when the tether is properly attached near the UAV center-of-mass. That said, the trajectory generator is designed to enact emergency return-to-home functionality should sustained, excessive pitching ever arise mid-flight.

Unlike the simulated external force estimation performance results in Fig. 12, the hardware results in Fig. 17 do not have a truth reference for the actual resultant forces caused by wind and the tether. However, a qualitative comparison between the simulation and hardware estimates points to the hardware system's ability to accurately deduce both when the tether is taut as well as when the UAV is grounded versus in the air. Moreover, no adjustment to the rough tether tautness threshold is needed due to the quality of the physical parameter matching between the simulated and hardware platforms.

Similarly to the simulation results in Fig. 13, Fig. 18 demonstrates that the hardware platform is able to perform the entire commanded 40-degree sweep angle despite wind disturbances. In the case of indoor flight testing, the limiting factor is the size of the flight space. Because the sweep operation is controlled in a low-bandwidth feedback loop by the trajectory planner using the estimated relative position, sweep angle ability is maintained in spite of wind disturbances and a lack of inner-loop attitude integrator control. However, at much higher relative wind speed levels, it will be necessary to implement a timeout method to ensure that the UAV does not get stuck perpetually fighting against wind disturbances that require roll angles greater than 30 degrees.

Indoor testing results with a combination of actual and spoofed sensing indicate that the constructed hardware platform achieves the same level of mission performance as the previously fine-tuned simulated platform. To achieve comparable performance in hardware, controller gain and Kalman filter covariance tuning are required; however, no appreciable re-writing of the code used in simulation is necessary. With hardware performance and simulation results validated, next steps include expanding on the results presented here with a moving base station, real-time outdoor GPS sensing, and wind velocity measurement with the omnidirectional air probe.

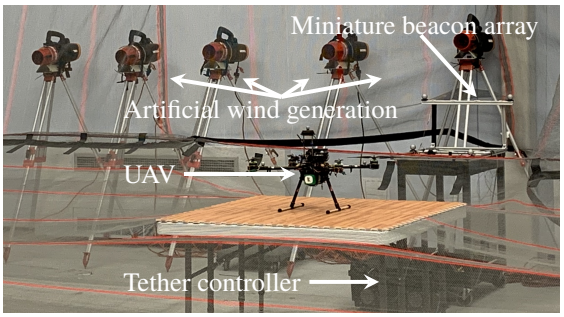

Fig. 14 Physical setup for the indoor flight test trials. The tether length for wake survey mode is 7 meters, and a 1:35 scale beacon array is used for real-time relative pose estimation via a combination of real and spoofed sensor data. Generated wind provides realistic wind disturbances despite a static $\mathcal{S}$-frame.

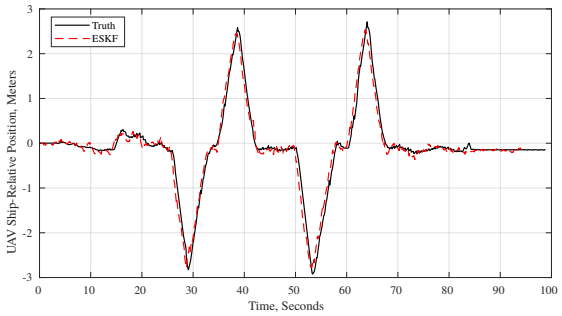

Fig. 15 Relative state estimate of UAV y position w.r.t. and expressed in $\mathcal{S}$ over the course of an entire indoor hardware flight test with multiple sweeps. Accurate estimation is facilitated by the fusion of spoofed differential GPS and real vision-based pose measurements.

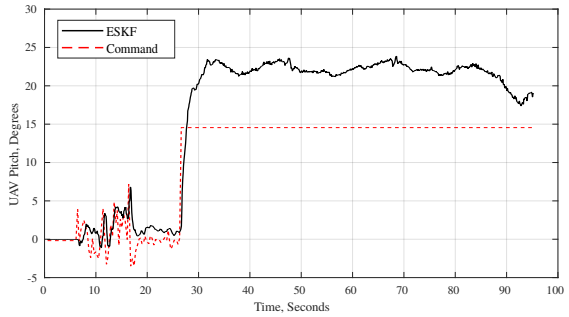

Fig. 16 UAV pitch tracking performance throughout an entire indoor hardware flight test with multiple sweeps. A steady-state pitch disturbance between 5 and 10 degrees is induced by the rotor blade flapping effect at a relative wind speed of 4-7 m/s, very similarly to observed simulation results in Fig. 9.

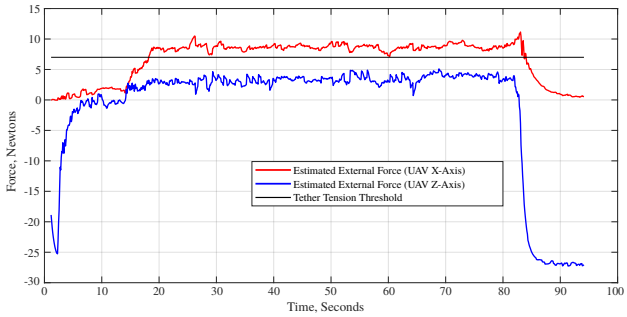

Fig. 17 Comparison between the x and z components of ${}^{\mathcal{B}}\boldsymbol{f}_{\text{ext}}$ versus ${}^{\mathcal{B}}\hat{\boldsymbol{f}}_{\text{ext}}$ for an indoor hardware flight. As with simulation results in Fig. 12, the estimated forces in the UAV b_x, b_z directions reveal the takeoff point at $\approx$ 3 s and the point of tether tautness at $\approx$ 20 s.

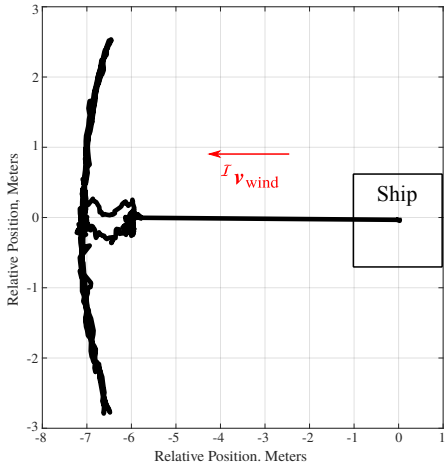

Fig. 18 Top view of a sweep trajectory from indoor flight testing with a tether length of 7 m and wind speed of 4-7 m/s.

VIII. Conclusion

This paper presents an UAS designed to obtain high-resolution air wake velocity data behind a cruising naval vessel through autonomous control with absolute and relative state estimation techniques that are tailored to the specific challenges of the maritime environment. The use of a tether affords a measure of passive flight stabilization which, when coupled with the outlined control strategy, allows the UAV to attain sufficient coverage to map both the predominantly turbulent and free stream regions of the air wake profile. The relative state estimation algorithm, which fuses measurements from a differential GPS as well as a vision-based pose estimation scheme using active IR beacons, provides a centimeter-level-accuracy estimate of the UAV state relative to the ship even at very large distances.

Extensive effort has gone into the creation and validation of a high-fidelity simulation environment that successfully models all relevant aspects of the measurement process, including the UAV, ship, tether, and wind dynamics. The simulation environment has allowed for the testing and validation of the UAS control and state estimation strategies, instilling confidence in the ability of the platform to obtain the desired air wake measurements on an actual Naval vessel even in the presence of significant headwind. In addition to extensive simulation testing, indoor flight tests further validate the state estimation and flight control schemes under real-world conditions and disturbances. Near-term future work for this project includes replicating the simulation results in outdoor environments, including obtaining real air wake measurements behind a moving ship for CFD model validation.

Acknowledgments

This research is funded with a Small Business Technology Transfer Grant from the Office of Naval Research through Creare LLC.

References

[1] Yuan, W., Wall, A., and Lee, R., "Combined numerical and experimental simulations of unsteady ship airwakes," *Computers & Fluids*, Vol. 172, 2018, pp. 29 – 53. https://doi.org/https://doi.org/10.1016/j.compfluid.2018.06.006, URL http://www.sciencedirect.com/science/article/pii/S0045793018303293.

[2] Dooley, G. M., Carrica, P., Martin, J., Krebill, A., and Buchholz, J., "Effects of Waves, Motions and Atmospheric Turbulence on Ship Airwakes," *AIAA Scitech 2019 Forum*, 2019. https://doi.org/10.2514/6.2019-1328, URL http://dx.doi.org/10.2514/6.2019-1328.

[3] Wang, X., Sarhaddi, D., Wang, Z., Mignolet, M., and Chen, P., "Modeling-based hyper reduction of multidimensional cfd data: Application to ship airwake data," *AIAA Scitech 2019 Forum*, American Institute of Aeronautics and Astronautics Inc, AIAA, 2019. https://doi.org/10.2514/6.2019-1850, aIAA Scitech Forum, 2019 ; Conference date: 07-01-2019 Through 11-01-2019.

[4] Tinney, C. E., Shipman, J., and Panickar, P., "Reduced-Order Models for Characterizing Ship Airwake Interactions," *2018 Fluid Dynamics Conference*, 2018. https://doi.org/10.2514/6.2018-3233, URL http://dx.doi.org/10.2514/6.2018-3233.

[5] Polsky, S. A., Wilkinson, C., Nichols, J., Ayers, D., Mercado-Perez, J., and Davis, T. S., "Development and Application of the SAFEDI Tool for Virtual Dynamic Interface Ship Airwake Analysis," *54th AIAA Aerospace Sciences Meeting*, 2016. https://doi.org/10.2514/6.2016-1771, URL http://dx.doi.org/10.2514/6.2016-1771.

[6] Shukla, S., Sinha, S., and Singh, S., "Ship-helo coupled airwake aerodynamics: A comprehensive review," *Progress in Aerospace Sciences*, Vol. 106, 2019, pp. 71 – 107. https://doi.org/https://doi.org/10.1016/j.paerosci.2019.02.002, URL http://www.sciencedirect.com/science/article/pii/S0376042118301453.

[7] SHI, Y., HE, X., XU, Y., and XU, G., "Numerical study on flow control of ship airwake and rotor airload during helicopter shipboard landing," *Chinese Journal of Aeronautics*, Vol. 32, No. 2, 2019, pp. 324 – 336. https://doi.org/https://doi.org/10.1016/j.cja.2018.12.020, URL http://www.sciencedirect.com/science/article/pii/S1000936119300329.

[8] Metzger, J., Snyder, M. R., Burks, J. B., and Kang, H. S., "Measurement of Ship Air Wake Impact on a Remotely Piloted Aerial Vehicle," 2012.

[9] Phelps, D., Gamagedara, K., Waldron, J., Patil, K., and Snyder, M., "Ship Air Wake Detection Using Small Fixed Wing Unmanned Aerial Vehicle," *2018 AIAA Aerospace Sciences Meeting*, 2018. https://doi.org/10.2514/6.2018-0784, URL http://dx.doi.org/10.2514/6.2018-0784.

[10] Mallon, C. J., Muthig, B. J., Gamagedara, K., Patil, K., Friedman, C., Lee, T., and Snyder, M. R., "Measurements of Ship Air Wake Using Airborne Anemometers," *55th AIAA Aerospace Sciences Meeting*, 2017. https://doi.org/10.2514/6.2017-0252, URL http://dx.doi.org/10.2514/6.2017-0252.

[11] Gamagedara, K., Patil, K., Lee, T., and Snyder, M. R., "Vision-Based Relative Localization for Airborne Measurements of Ship Air Wake," *2018 AIAA Atmospheric Flight Mechanics Conference*, 2018. https://doi.org/10.2514/6.2018-0527, URL http://dx.doi.org/10.2514/6.2018-0527.

[12] Kumar, A., and Ben-Tzvi, P., "Novel wireless sensing platform for experimental mapping and validation of ship air wake," *Mechatronics*, Vol. 52, 2018, pp. 58–69.

[13] Khithov, V., Petrov, A., Tishchenko, I., and Yakovlev, K., "Toward Autonomous UAV Landing Based on Infrared Beacons and Particle Filtering," *Robot Intelligence Technology and Applications 4*, 2016, p. 529–537. https://doi.org/10.1007/978-3-319-31293-4_43, URL http://dx.doi.org/10.1007/978-3-319-31293-4_43.

[14] Kalinov, I., Safronov, E., Agishev, R., Kurenkov, M., and Tsetserukou, D., "High-Precision UAV Localization System for Landing on a Mobile Collaborative Robot Based on an IR Marker Pattern Recognition," *2019 IEEE 89th Vehicular Technology Conference (VTC2019-Spring)*, 2019. https://doi.org/10.1109/vtcspring.2019.8746668, URL http://dx.doi.org/10.1109/VTCSpring.2019.8746668.

[15] Stanford Artificial Intelligence Laboratory et al., "Robotic Operating System," , ???? URL https://www.ros.org.

[16] Tagliabue, A., Kamel, M., Verling, S., Siegwart, R., and Nieto, J., "Collaborative transportation using MAVs via passive force control," *2017 IEEE International Conference on Robotics and Automation (ICRA)*, 2017, pp. 5766–5773.

[17] Jackson, J., Ellingson, G., and McLain, T., "ROSflight: A lightweight, inexpensive MAV research and development tool," *2016 International Conference on Unmanned Aircraft Systems (ICUAS)*, 2016, pp. 758–762.

[18] Cutler, M., Michini, B., and How, J. P., "Lightweight infrared sensing for relative navigation of quadrotors," *2013 International Conference on Unmanned Aircraft Systems (ICUAS)*, 2013, pp. 1156–1164.

[19] Faessler, M., Mueggler, E., Schwabe, K., and Scaramuzza, D., "A monocular pose estimation system based on infrared LEDs," *2014 IEEE International Conference on Robotics and Automation (ICRA)*, 2014. https://doi.org/10.1109/icra.2014.6906962, URL http://dx.doi.org/10.1109/ICRA.2014.6906962.

[20] Draper, B., "Long-range outdoor monocular localization with active features for ship air wake measurement," Master's thesis, Massachusetts Institute of Technology, Cambridge, Massachusetts, 2019.

[21] Solà, J., "Quaternion kinematics for the error-state Kalman filter," *CoRR*, Vol. abs/1711.02508, 2017. URL http://arxiv.org/abs/1711.02508.

[22] Berman, Z., "Outliers rejection in Kalman filtering; Some new observations," *2014 IEEE/ION Position, Location and Navigation Symposium - PLANS 2014*, 2014. https://doi.org/10.1109/plans.2014.6851466, URL http://dx.doi.org/10.1109/PLANS.2014.6851466.

[23] Hoffmann, G., Huang, H., Waslander, S., and Tomlin, C., "Quadrotor Helicopter Flight Dynamics and Control: Theory and Experiment," *AIAA Guidance, Navigation and Control Conference and Exhibit*, 2007. https://doi.org/10.2514/6.2007-6461, URL http://dx.doi.org/10.2514/6.2007-6461.

[24] Klinker, M., "Tethered UAV Flight using a Spherical Position Controller," Master's thesis, Massachusetts Institute of Technology, Cambridge, Massachusetts, 2016.

[25] Rankin, J., "An error model for sensor simulation GPS and differential GPS," *Proceedings of 1994 IEEE Position, Location and Navigation Symposium - PLANS'94*, 1994, pp. 260–266.